Applied Catalysis B: Environmental 237 (2018) 416–423

Contents lists available at ScienceDirect

Applied Catalysis B: Environmental

journal homepage: www.elsevier.com/locate/apcatb

Enhanced visible light catalytic activity of $MoS_2/TiO_2/Ti$ photocathode by hybrid-junction

Chaoqun Cheng[a], Guohua Liu[b], Kang Du[a], Gang Li[c], Wendong Zhang[c], Simone Sanna[d], Yunzhong Chen[d], Nini Pryds[d], Kaiying Wang[a,*]

[a] Department of MicroSystems, University of South-Eastern Norway, Horten 3184, Norway
[b] State Key Laboratory of Alternate Electrical Power System with Renewable Energy Sources, North China Electric Power University, Beijing, 102206, China
[c] Micro and Nano System Research Center, Key Lab of Advanced Transducers and Intelligent Control System (Ministry of Education) & College of Information Engineering, Taiyuan University of Technology, Taiyuan, 030024, China
[d] Department of Energy Conversion and Storage, Technical University of Denmark, Risø Campus, 4000, Roskilde, Denmark

ARTICLE INFO

Keywords:
Hybrid-junction
Water splitting
Titanium dioxide
Z-scheme
Molybdenum disulfide

ABSTRACT

In photoelectrochemical (PEC) water splitting systems, crucial obstacles limiting their performance are poor charge carrier dynamics and high recombination rate of photoexcited electron-hole pairs. Here, we report that this issue can be alleviated by engineering a hybrid-junction that is composed of homo- and hetero- junctions. This strategy is performed by facile hand-spraying MoS_2 over the surface of anatase/rutile homo-junction TiO_2 film on the Ti substrate to further form a hybrid-junction photocathode. By applying this photocathode into PEC reactor, enhanced catalytic activity is achieved under visible light (AM1.5 illumination of 300 W/m^2) with hydrogen evolution reaction (HER) potential of −114 mV versus reversible hydrogen electrode (RHE) at 10 mA/cm^2 and long-term stability of more than 10 times improvement comparing to ordinary electrode without the introduction of hybrid-junction. The hybrid-junction that effectively regulates charge separation and transfer pathways is proven to be responsible for the enhanced activity. As a novel exploration, this hybrid-junction system comprising of low-cost, efficient charge separation and transfer, and visible light responsivity offers a new path for relative materials to boost their PEC performance.

1. Introduction

Photoelectrochemical (PEC) water splitting system harvesting sunlight to drive uphill water splitting reactions has been the focus of attention due to its potential of converting sunlight into chemical fuels in a cost-economical and sustainable way [1–4]. In the past decades excellent advancement has been achieved, specially the metal oxide semiconductor has been invested greatly due to their intrinsic nature of the d orbital states, earth-abundance and superior PEC performance [5–8]. However, their PEC performance to the practical commercialization is still subjected to the limitations of poor charge-carrier dynamics and high recombination rate issues under the solar illumination [9,10]. To solve these issues, some efforts have been made to pursue reliable strategies in particular the search for hybrid systems [3,11–13].

Hetero- and homo-junctions are two distinctive approaches used in the hybrid systems [14,15]. The designing of hetero-junction is a well-established approach as it holds great potential to overcome the drawbacks of serious charge recombination and limited visible-light utilization [16], typically involving building an advanced two-step (Z-scheme) system. The Z-scheme system composed of two semiconductors with desired band gaps and energy positions ensure that the separated electrons and holes transport only in opposite directions toward the surface for preferred reactions, minimizing deleterious recombination and undesirable side reactions [17,18]. Z-scheme construction can not only regulate charge transfer pathways but also increase the sunlight utilization through the series connected two semiconducting materials with narrow bandgap absorbing visible light [19,20]. As an example, there have been reports that Z-scheme hetero-junction of MoS_2/TiO_2 with CdS quantum dots can effectively improve the catalytic activities under the visible light irradiation as the result of beneficial charge interaction in the interface [21]. Recent studies have also demonstrated that the excellent catalytic activity in the heterojunctions of MoS_2/TiO_2 is related to the strong interaction between the MoS_2 and TiO_2 [22–27].

On the other hand, the construction of homo-junction (phase-junction) is an alternative configuration access to charge-carrier separation because the formation of homo-junction between two distinct phases can adjust the transport of the charge carriers along the inter-phases band alignment [9]. For example, it has been reported that surficial

* Corresponding author.
E-mail address: Kaiying.Wang@usn.no (K. Wang).

https://doi.org/10.1016/j.apcatb.2018.06.012
Received 15 April 2018; Received in revised form 31 May 2018; Accepted 3 June 2018
Available online 05 June 2018

phase-junction between the nanoparticles of anatase and rutile TiO_2 can enhance the water splitting activities [28]. The basic mechanism is that the surficial anatase/rutile phase junctions can guide the electrons or holes transferred between band structures of rutile and anatase TiO_2, thereby facilitating separation of electron-hole pairs and catalytic activities [28–30].

Although configuring hetero-junction or homo-junction is well explored, the potentials of integrating hybrid-junction comprising of hetero-junction and homo-junction into a single photoelectrode is still lack of investigation, especially in terms of the impact on charge carrier dynamics. In the heterogeneous system, the doping of foreign elements [31–33] was explored to provide multi-channel paths for improving the charge-carrier dynamics. In this study, we propose a facile strategy of building hybrid-junction to improve the catalytic activity of photocathode under visible light. We demonstrate that integration of homo-junction and hetero-junction on the bulk metal substrate as a simple but effective strategy could effectively fast the performance of charge separation, transfer and transportation dynamics at the interface and reduce charge carrier recombination in the bulk and at the surface.

We fabricated hybrid-junction of MoS_2/TiO_2 by hetero-coupling MoS_2 and homo-junction (mixed-phases) TiO_2 on the substrate of Ti foil. The hybrid-junction MoS_2/TiO_2 exhibits high activities under a visible light irradiation (AM 1.5 G illumination of 300 W/m^2) with hydrogen evolution reaction (HER) potential of −114 mV versus reversible hydrogen electrode (RHE) at 10 mA/cm^2, as well as long-term stability for more than 12 h at -0.3 V vs RHE while comparing to about 1 h without the introduction of hybrid-junction under same measurement conditions, more than 10 times improvement. The homo-junction TiO_2 thin layer on the substrate of Ti was synthesized through simple one-step thermal annealing process, different from traditional synthesis using hydrothermal or sol-gel methods [34–36]. The characterization on the HER activities suggest the homo-junction TiO_2 on the substrate of Ti could facilitate charge separation and transportation under the visible light illumination. After the hetero-coupling with MoS_2 constructed as hybrid-junction system, this cathode composite of MoS_2/TiO_2 on the substrate Ti exhibit higher activity and stability during the HER. The underlying charge transfer analysis elucidated that the hybrid-junction of Z-scheme hetero-junction and homo-junction plays important roles in the excellent performance.

2. Experimental section

2.1. Materials

Commercially Molybdenum disulfide (MoS_2) microflakes liquid-spraying was purchased from CRC Industries Americas Group. Titanium foils (Ti foils, 30 mm × 14 mm × 0.5 mm, 99.8% purity) were cut out from Ti sheet, which was purchased from Baoji Titanium Industry Co., LTD. Ethanol, acetone, isopropanol and deionized water were obtained from Sigma-Aldrich without further purification.

2.2. Preparation of homo-junction TiO_2 and MoS_2/TiO_2 composite electrodes

The fabrication consists of oxidation, spraying and annealing processes. Initially, Ti foils were cleaned by immersing the foils into the acetone rinsed by ultrasonic bath and subsequently dried in flowing nitrogen gas. After the initial cleaning step, Ti foils were oxidized at 400, 500 and 600 ℃ for 2 h with oxygen gas continually flowing through the quartz tube furnace to generate a thin layer of homo-junction TiO_2 on the surface of the Ti foil (Fig. S1). Following the oxidation step, commercial lubricating MoS_2 spray (CRC Industries) was applied to the TiO_2/Ti, followed by baking at 100 ℃ in the oven with ambient atmosphere for 10 h to ensure that all the solvent is evaporated. In the last annealing process, the pristine MoS_2/TiO_2/Ti foils were annealed at 500 ℃ for 1, 2, and 3 h, respectively in Nitrogen atmosphere under ambient pressure and cooled to the room temperature.

2.3. Physical characterization

Surface morphology of as-prepared samples was examined by field emission scanning electron microscopy (FESEM) (Hitachi, SU 8230) equipped with energy-dispersive X-ray spectrum (EDS) and electron backscatter diffraction (EBSD) microstructural-crystallographic characterization. Atomic force microscopy (AFM, Parker XE 200) was used to visualize surface the topography of samples on the nanometer scale. UV–vis light absorption spectra of the as-prepared samples were obtained using a SHIMADZU, UV-2600 spectrophotometer equipped with an integrated sphere assembly using diffuse reflection method. $BaSO_4$ was used as a reference to measure all samples in the wavelength range of 250–800 nm with a slit width of 1 nm. X-ray diffraction (XRD) patterns were collected on a Bruker D8-Advance diffractometer using Cu Kα radiation (λ = 1.5405 Å) in a range of 2-80° at a scan rate of 5°/min. Photoluminescence (PL) spectra were performed in the FS5 Spectrofluorometer of Edinburgh Instruments by focusing the laser radiation centered at 400 nm from an Xeon lamp onto the samples.

2.4. Photoelectrochemical measurement

PEC/Electrochemical measurements with/without simulated solar light illumination were performed and evaluated in a standard PEC three electrodes setup which is connected to electrochemical workstation (Zahner Elektrik IM6). The incident light was filtered through AM 1.5 G solar simulator over an adjustable 500 W Xeon lamp (AM 1.5 G, 300 W/m^2). The as-prepared composites, platinum gauze and Ag/AgCl with saturated KCl solution were used as working, counter and reference electrodes. In the text, the measured potentials *vs.* Ag/AgCl were all changed to the RHE scale based on the Nernst equation: $E_{RHE} = E_{Ag}/E_{AgCl} + pH * 0.059 + 0.1976$. All the current density reported in the work were calibrated using IR compensation, where the R (resistivity) was estimated by electrochemical impedance spectroscopy (EIS) with a frequency ranging from 10 Hz to 1 M Hz.

Linear scanning voltammetry measurements were carried out in 0.5 M H_2SO_4 at a constant scan rate of 20 mV/s over the potential range of -0.6 - 0 V (vs RHE). A long-term stability test for MoS_2/TiO_2 and MoS_2/Ti were conducted by an extended electrolysis (15 h) under dark or light conditions at a constant reduction potential of -0.3 V vs RHE. EIS test was carried out at open-circuit potential by applying an AC potential with an amplitude of 50 mV during the frequency range of 4×10^5 to 10^{-3} Hz in 0.5 M H_2SO_4 with/without the AM 1.5 G illumination (300 W/m^2). Mott-Schottky plots were obtained at frequencies of 5, 10 and 15 kHz and amplitude of 10 mV in 0.5 M H_2SO_4 solution under the dark or light conditions. In addition, current density-voltage (J-V) characteristic in an anodic direction was acquired at a scan rate of 20 mV/s. The measurements were carried out in a solution of Na_2SO_4 (pH 6.8) and subsequently in another solution of 1 M KOH (pH 13).

3. Results and discussion

3.1. Homo-junction TiO_2 on the substrate of Ti

Homo-junction TiO_2 was synthesized on the surface of Ti foil using simple one-step annealing process, as presented in the experimental section. The presence of homo-junction (mixed-phases) TiO_2 on the surface of Ti foil after the annealing process was determined by X-ray diffraction (XRD) and electron backscatter diffraction (EBSD). Fig. 1a shows the XRD patterns of TiO_2 at the temperature ranging from 400 ℃ to 600 ℃, in which both anatase or rutile TiO_2 could be observed (Fig. S2). Fig. 1b presents the EBSD mapping, clearly showing the mixed-phases orientation mapping on the surface with assorted colors.

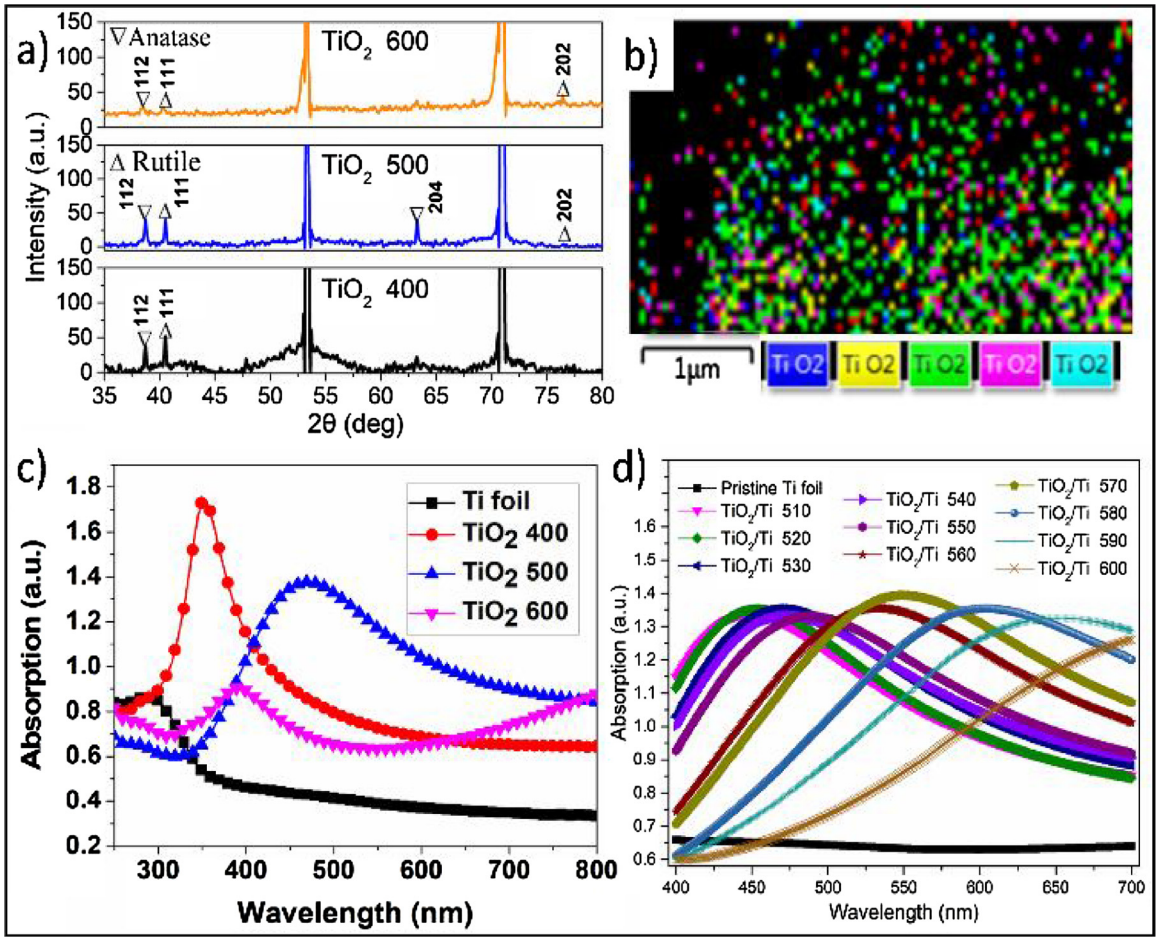

Fig. 1. a) XRD patterns of the as-prepared samples. b) Orientation map of mixed-phases TiO_2 marked with assorted colors using EBSD microstructural crystallographic technology. More parameters refer to Fig. S3 (Table S1, S2 and S3). (c) Ultraviolet-visible (UV–vis) absorption spectrums of all samples TiO_2/Ti after 2 h annealing process at respective 400, 500 and 600 °C. (d) UV–vis absorption spectra of a group of TiO_2/Ti samples after 2 h of annealing under varied temperature with distinct visible light absorption bandwidth.

Fig. 1c shows the UV–vis absorption spectra, indicating a strong resonant visible light absorption peak around 480 nm at 500 °C [37–40]. Fig. 1d further shows the UV–vis absorption spectra, in which the absorption edge wavelength of material moves to the infrared light area in the direction of longer wavelength as the processing temperature increases gradually, confirming the dependence of resonance absorption wavelength on the microscopic changes of surficial mixed-phases TiO_2 induced by the elevated thermal treatment in the temperature range (Fig. S4) [37,41].

Fig. 2 show *J-V* plots of proton reduction with/without AM 1.5 G illumination and corresponding Tafel slope values. Figs. 2a-c show *J-V* curves measured in dark and light respectively. As seen from these figures, TiO_2/Ti (400 °C) and TiO_2/Ti (500 °C) exhibit better reduction activities under the light condition, while TiO_2/Ti (600 °C) itself shows a poor reduction current under the light, even worse than that in dark. This difference is consistent with the differential absorption spectra in the Fig. 1c. For the TiO_2/Ti (500 °C), an overpotential of 216 mV at 10 mV/cm^2 was achieved under the application of light, almost 50% improvement comparing to the 403 mV under the dark condition, suggesting that TiO_2/Ti (500) has better PEC activities in the visible light range. Fig. 2d presents the Tafel slope for the TiO_2/Ti under the dark and light, in which the TiO_2/Ti (500 °C) has a lower Tafel slope value of 159 mV/decade, and thus was better activity than the others. Since the Tafel slope value is close to the Volmer reaction regime (120 mV/decade) [42,43], the rate-limiting step here is the electrochemical adsorption step due to a limited amount of surface active sites.

3.2. Hybrid-junction $MoS_2/TiO_2/Ti$ electrode

The investigation suggests that the homo-junction TiO_2 on the substrate of Ti has favorable charge transfer features under the visible light illumination but is restricted by the deficient surface sites which could increase the rate of interfacial charge transport. To eliminate the deficit, the homo-junction TiO_2 was covered by hand-spraying thin layer of commercial MoS_2, forming a functional complementary hetero-junction system. In addition to the merits of containing no precious metals and earth abundance, MoS_2 with large amount of edges could also offer enough active sites for HER activities [7,44]. The commercial MoS_2 nanoflakes liquid-spraying received our attention due to the universal of this method enabling easy-fabricating hetero-junction system. Fig. 3(a) shows the facile and cost-efficient processes for fabricating the novel hybrid-junction MoS_2/TiO_2. All the prepared samples at different processes are noted respectively as Ti (**A**), homo-junction TiO_2/Ti (**B**), pristine MoS_2/TiO_2/Ti (**C**) and annealed MoS_2/TiO_2/Ti (1 h/2 h/3 h) (**D**/**E**/**F**).

Fig. 3(b) shows SEM top-view images of the TiO_2 (sample **B**), pristine MoS_2/TiO_2/Ti (noted as MoS_2/TiO_2, sample **C**) and annealed MoS_2/TiO_2/Ti (MoS_2/TiO_2, sample **D**, **E** and **F**). The morphology of the materials TiO_2 on the surface is shown in Fig. 3 (b)-**B**. The as-received (without thermal treatment) pristine MoS_2 shows rough and irregular surface morphology. Upon annealing at 500 °C in the nitrogen atmosphere, much more dense structure with small pores on the surface is observed in the sample **E**, mainly due to the thermal treatment which crystalizes the surficial MoS_2 microflakes [43]. Favouring the specific

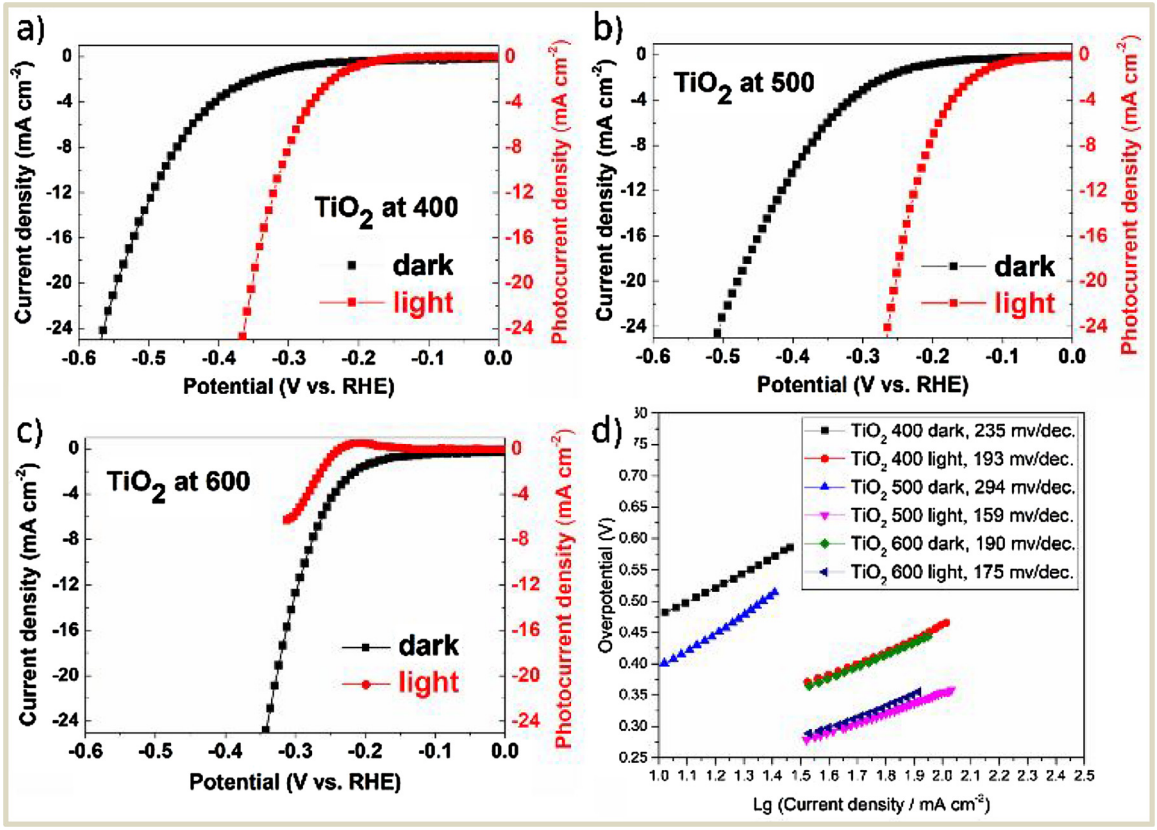

Fig. 2. (a–c) Room-temperature *J-V* curves of the TiO_2/Ti measured in 0.5 M H_2SO_4 under respective dark and light with AM 1.5 G illumination (300 W/m^2). (d) Tafel plots corresponding to the HER polarization curves and related data for the samples.

surface area, these top-porous networks offer more edge sites allowing for HER reactions [45]. Furthermore, the thin layer of continuous network structure on the surface provides an accessible tunnel for light penetrating to the inner part of TiO_2. After longer annealing time, the undersigned damage to the surface structure could be observed as the potholes in the surface of sample **F**. Fig. S6 show the energy dispersive X-ray spectroscopy (EDS) mapping, confirming that the Ti, O, Mo, and S species existed in the multi-layered film composites. To verify the thickness of MoS_2 and the MoS_2 wrapped on the surface of particles, a cross-sectional FESEM analysis was conducted (Fig. S7a, b). The FESEM images show distinct wrapping of MoS_2, with measured thickness of 1.30 u m (MoS_2 pristine) and 400 nm (MoS_2 2 h). Element-specific analysis was performed by the dedicated Line-scan EDS along the direction of bottom to surface (Fig. 1c), indicating existence of the material of MoS_2. The morphology of MoS_2 wrapped on the surface of particles was further confirmed by AFM surface topology (Fig. S7d).

Fig. 3(c) shows the XRD patterns of five as-prepared hybrid-junction samples. Before spraying MoS_2, the peaks of (112) and (204) facets of anatase TiO_2 and (111) facet of rutile TiO_2 could be observed in Fig. 3(c)-B (Anatase PDF 00-021-1272; Rutile PDF 00-021-1276). After annealing, the diffraction characteristic peaks of TiO_2 are still observed in the patterns of MoS_2/TiO_2 composites with grown crystallite size and strength after the thermal treatment. The peaks centered at 26° and 28.7° can be assigned to (101) facet of anatase TiO_2 and (110) facet of rutile TiO_2 (Anatase PDF 00-021-1272; Rutile PDF 00-021-1276). For MoS_2, the detected signals located at 29.5°, 44.6° and 60.5° are assigned to (004), (006) and (110) (MoS_2 PDF 01-087-2416) respectively with increased crystallinity along with increasing annealing temperature [46]. The crystal phase information on the TiO_2 and MoS_2 suggests the hetero-junction composite consisting of MoS_2 and mixed-phases TiO_2 based homo-junction.

The HER activities of MoS_2/TiO_2 were measured and compared with that of the MoS_2/Ti. Fig. 4a presents photo-current of the obtained dark-current and photo-current (Fig. S8(a–c)), in which the MoS_2/TiO_2 (500 ℃ 2 h) exhibited higher photo-current during the HER under the light irradiation than the rest, and excellent HER activities with overpotential of −114 mV at 10 mA/cm^2. The improved overpotential is much lower than that of latest reports, such as 0D(MoS_2)/2D(g-C_3N_4) heterojunctions (about -450 mV at 2 mA/cm^2) [18], a-MoSx@MPA colloidal nanodots (about −270 mV at 5 mA/cm^2) [47] and high-percentage 1 T-phase MoS_2 nanodots (about −180 mV at 10 mA/cm^2) [48]. It is even comparable to that of MoS_2 with multifunctional active sites (around −100 mV at 10 mA/cm^2 in 1.0 M aqueous KOH) [49]. To examine the role of homo-junction TiO_2 in the hetero-junction, the HER activities of MoS_2/Ti without introducing homo-junction TiO_2 was also measured. Fig. S8d shows the current density under the dark and light condition during the HER for the MoS_2/Ti. The current density under the light is almost overlapped with the current density under the dark, indicating a poor visible light utilization. Thus, the homo-junction TiO_2 plays a crucial role on promoting the HER activities of MoS_2/TiO_2 after thermal treatment. Fig. 4b presents the Tafel slope for the MoS_2/TiO_2 (500 ℃ 2 h), with a value of 99 mV/decade under the light, much lower than the Tafel slope value 159 mV/decade of TiO_2/Ti shown in the Fig. 2d. The Tafel slope value is much closer to the Heyrovsky reaction regime (40 mV/decade), therefore the rate-limiting step is changing from the electrochemical adsorption step to the desorption step due to the covered MoS_2 [43]. In addition, in contrast to the HER activities of singular TiO_2 (TiO_2/Ti, Fig. 2c) and MoS_2 (MoS_2/Ti, Fig. S8d), the hetero-junction of MoS_2/TiO_2 exhibits lower overpotential and higher current under the light, suggesting that the hetero-junction interface between the homo-junction TiO_2 and MoS_2 also contributed to the charge separation and transfer, and then hastened the reaction kinetics.

A long-time stability test for MoS_2/TiO_2 (500 ℃ 2 h) was also carried out. Fig. 4c shows the current density measured during an

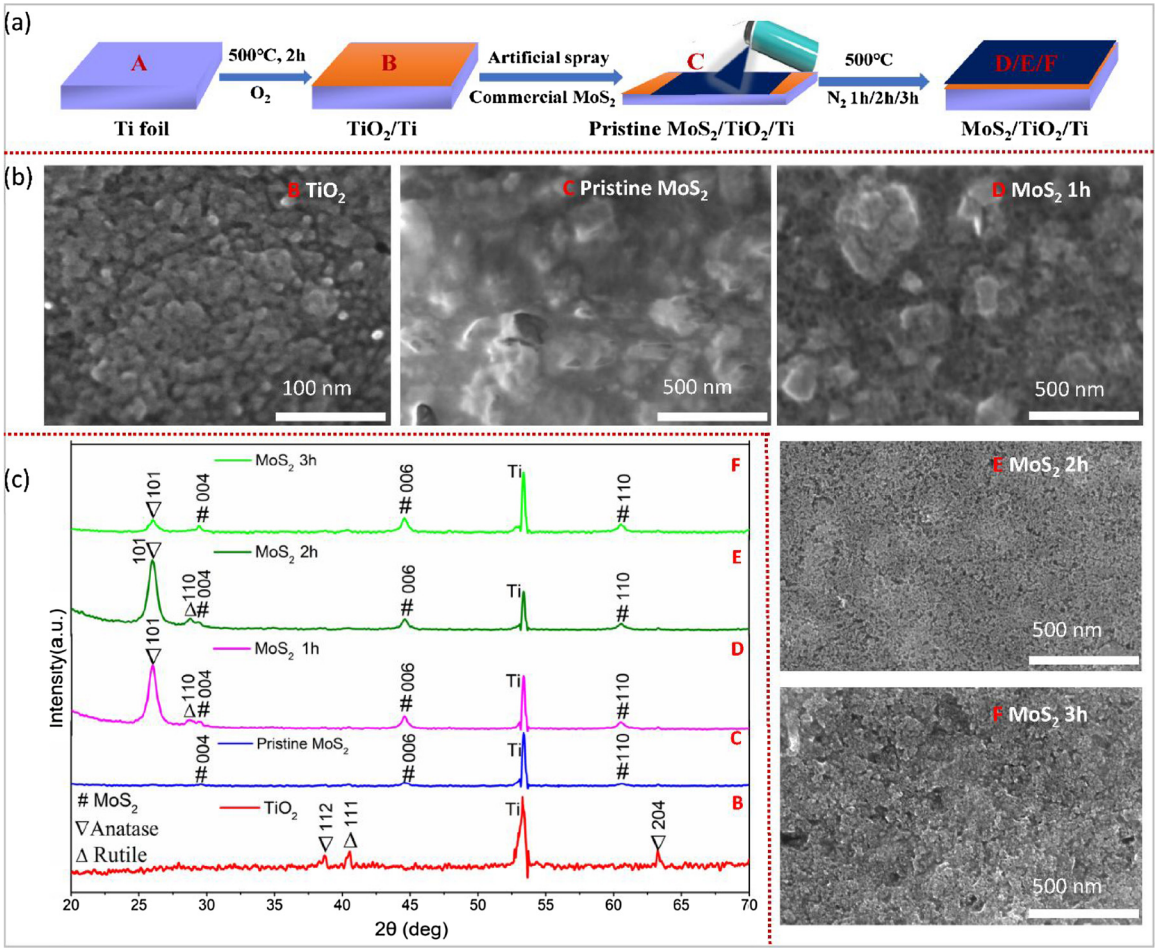

Fig. 3. (a). Schematic fabrication processes of all samples. Five kinds of samples involved in the experiments: Ti foil (sample **A**), TiO_2/Ti (sample **B**), pristine MoS_2/TiO_2/Ti (sample **C**), and annealed MoS_2/TiO_2/Ti in nitrogen atmosphere at temperatures of 500 °C (1 h/2 h/3 h) (sample **D**/**E**/**F**). The corresponding SEM images (b) and X-Ray diffraction patterns (c) of the as-received samples.

extended electrolysis (15 h) under the light at constant potential of −0.3 V (vs RHE), in which only 5% current density decay was observed after 12-hours continuous test under the light for the MoS_2/TiO_2 (500 °C 2 h). For comparison, Fig. 4d and Fig. 4e present the stability test for both MoS_2/TiO_2 without illumination and MoS_2/Ti with illumination. Almost 30% current decay was obtained for the MoS_2/Ti under the light, demonstrating a faster degradation rate than that of MoS_2/TiO_2 with/without illumination.

Fig. 4f further shows the HER polarization curves before and after 10 h stability test for the MoS_2/TiO_2 with/without the light, in which the current curve under the dark after 10 h stability measurement displays similar and repeatable features as the initial test before stability test. While a larger deviation in the current was observed under the light condition, indicating that the stability under the light is slightly weaker than that under the dark. We attribute the reason for the stability difference between the dark and the light to the photoinduced corrosion process on the edge sites or defect sites of the MoS_2 under the light exposure [50], because the faster and stronger reactions happened during the HER under the light. EIS was used to examine the impedance difference. Fig. S9 shows the EIS plots, in which a smaller semicircle of the arc line was exhibited for the MoS_2/TiO_2 (500 °C 2 h) under the light comparing to that under the dark, indicating better interfacial charge-transfer kinetics [43,44]. Meanwhile, a concave arc-line representing intense diffusion of ions of the interface between electrolyte and electrode was observed for the MoS_2/Ti under the light [51,52], suggesting poor charge-transfer property which is in agreement with the weak PEC activities. It should be noted that the high stability of the hybrid-junction of MoS_2/TiO_2 is comparable to other reported junctions such as MoS_2/TiO_2, nanojunction of (001) Facets MoS_2/Anatase TiO_2 (cyclic H_2 production for 9 h) [53], heterojunction of MoS_2/anatase TiO_2 (recycle degradation of MB for 5 h) [4], and MoS_2/TiO_2 Edge-On Heterostructure (12 h recycling photocatalytic H_2 evolution with intermittent evacuation) [26].

3.3. Discussion

Fig. S10 a,b shows the UV–vis absorption spectra of TiO_2 and MoS_2 respectively, in which the absorption edges of TiO_2 and MoS_2 were found to be 760 and 990 nm respectively, corresponding to the direct band gap energy (E_g) of 1.63 eV and 1.25 eV derived from Beer–Lambert law [37] as shown in the Fig. S10c. The narrower bandgap energy of homo-junction TiO_2 compare with the pure anatase phase (3.20 eV) and rutile phase of TiO_2 (3.03 eV) [54] could be attributed to the monolithic homo-junction TiO_2. To further understand the band positions, Fig. S11 presents the Mott-Schottky plots of the TiO_2 and the MoS_2/TiO_2 (500 °C 2 h) (the inset in Fig. S11), in which the positive slopes of Mott-Schottky indicate n-type TiO_2 and MoS_2 [55]. The labeled flat-band potentials are pointing at the difference between Fermi levels and water-oxidation potentials. We assumed that the Fermi levels were close to the conduction band, ignoring the slight difference between the Fermi levels and conduction band which has no effect on the analytical conclusion. Based on this, we propose an energy diagram of charge-carrier generation, separation and migration processes for the hybrid-junction MoS_2/TiO_2 on the Ti substrate as illustrated in Fig. 5.

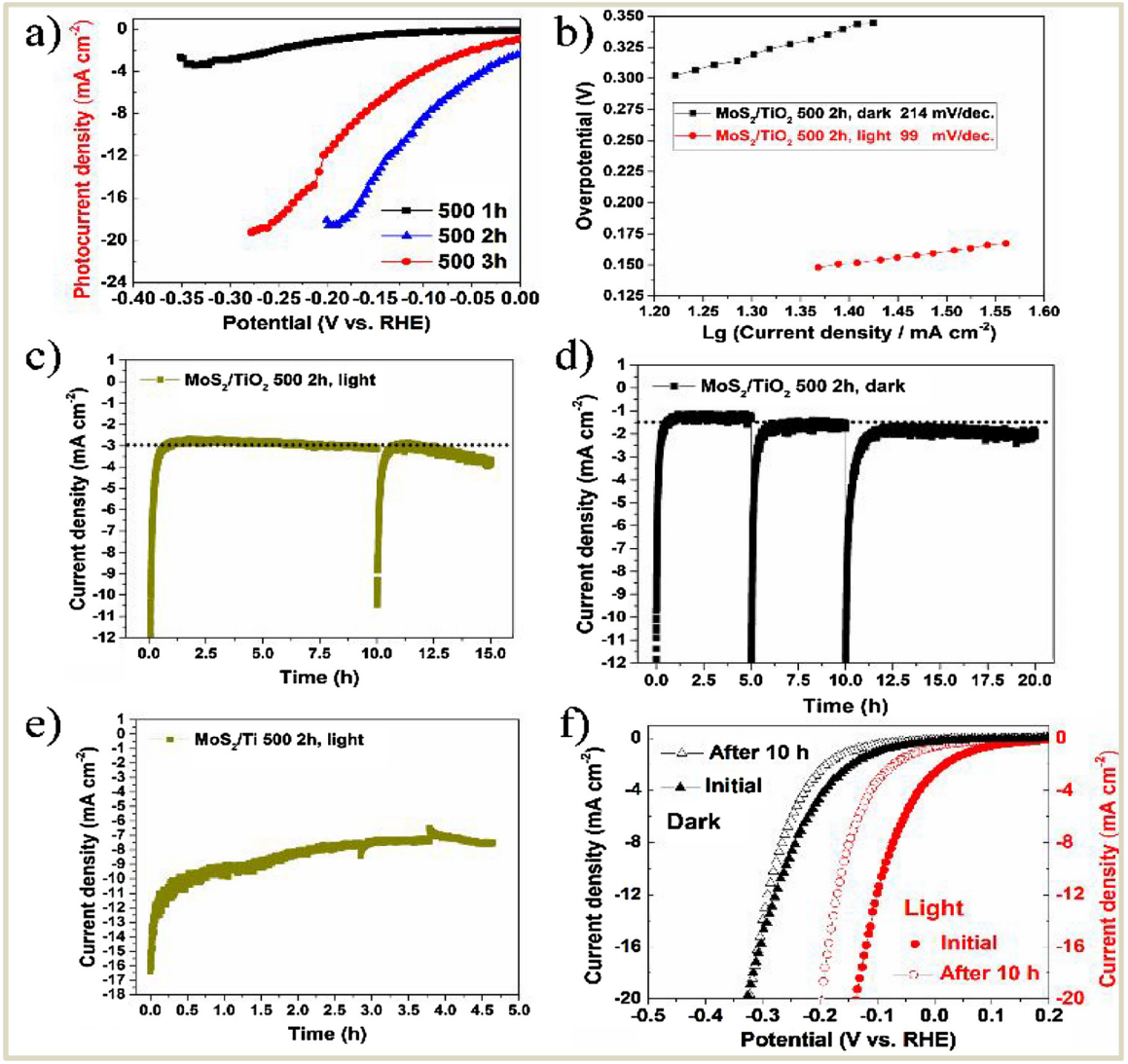

Fig. 4. (a) Polarization curves for the composites of MoS_2/Ti, measured in 0.5 M H_2SO_4 at a scanning rate of 20 mV/S under the light. (b) The corresponding Tafel plots and related data for the MoS_2/Ti (500 2 h). The long-term stability test for (c) the MoS_2/Ti (500 ℃ 2 h), (d) MoS_2/TiO_2 under the dark and (e) MoS_2/Ti under the light, respectively, during the HER at -0.3 V vs RHE for 15 h. (f) The HER polarization curves of the MoS_2/Ti (500 2 h) measured before and after the 10 h stability test at 20 mV/S. The figure of 500 in the figures all refers to the temperature of 500 ℃.

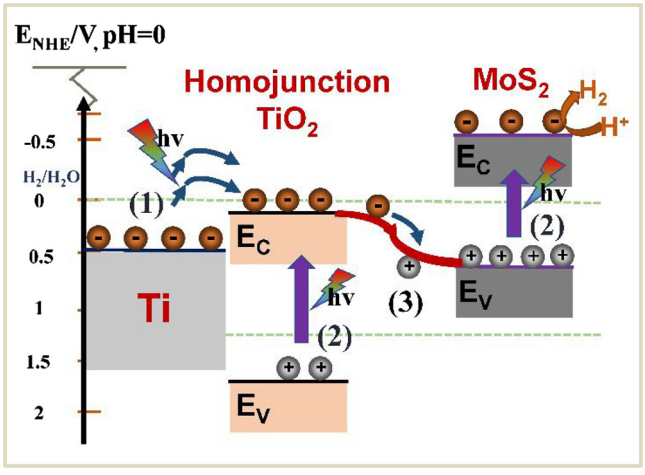

Fig. 5. Energy diagram of charge-carrier generation, separation and transportation processes for the hybrid-junction MoS_2/TiO_2 on the Ti substrate. (1) Plasmons assisted charge-carrier injection; (2) band-gap enabled excitation of charge-carrier; (3) Z-scheme mechanism of charge-carrier transportation.

The detailed Z-scheme mechanism are illustrated in the Fig. S12 and explained as follows.

In general, the MoS_2/TiO_2 composite shall be working as typical staggered gap (type II) heterojunction under usual double paths of charge transferring [56–59]. Guided by the matched bending band between the MoS_2 and TiO_2, an inner potential difference induced electric field would be created. The electrons from the conduction band (CB) of MoS_2 could transfer to the CB of TiO_2; in the meantime, the holes would tend to transfer from the valance band (VB) of TiO_2 to the VB of MoS_2. Given the fact that the CB potential of homo-junction TiO_2 is more positive than the standard proton reduction potential of H_2/H_2O (0.00 V Vs NHE), thereby protons cannot be thermodynamically reduced to hydrogen. Similarly, since the VB potential of MoS_2 is more negative than that of O_2/H_2O (1.23 V Vs NHE), thus the oxygen evolution reaction is prohibited. However, enhanced HER activities and stability were achieved in the work. Therefore, it is proposed that a direct Z-scheme catalytic mechanism is established. Under the mechanism, the built-in static electric field would guide the electrons from the CB of homo-junction TiO_2 transferring to the interface to combine with the active holes from the VB of MoS_2, thus preventing the electrons in the CB of homo-junction TiO_2 from the strong reducibility and the

holes in the VB of MoS_2 from the oxidizability. Thus, an enhanced HER activities could be achieved on the hybrid-junction of MoS_2/TiO_2 [60].

For the hetero-junction of MoS_2/TiO_2, to further ascertain that the underneath homo-junction TiO_2 on the substrate of Ti still has resonant visible light responsivity during the HER, we applied the linear sweeps *(J-V)* in anodic direction as shown in Fig. S13 under the dark. The oxygen evolution reactions (OER) was observed as gas bubbles in the electrolytes. Note that, once the gas bubbles were generated out of the surface, the surficial MoS_2 would delaminate from the surface due to the fact that the OER just taking place on the active sites of inner TiO_2. Once irradiated by light, the observed delamination process became much more severe so that deteriorating of MoS_2 flakes was observed. The reason could be due to the TiO_2 harvesting light energy resulted in the accelerated OER. These findings confirm that the ions and visible light can interacting with the underneath TiO_2, possibly owing to surficial porous MoS_2. Therefore, the underneath homo-junction TiO_2 on the substrate of Ti could absorb the visible light and convert the light energy during the catalytic reactions.

The interface between the TiO_2 and Ti in the hetero-junction of $MoS_2/TiO_2/Ti$ also plays an important effect on the overall charge carriers transfer and separation while restraining the recombination which resulted in the photoluminescence (PL) signal. Thus, PL emission spectra were recorded (Fig. S14) to probe the behavior of the interface. Comparing to the PL intensity of Ti substrate, much weaker intensity of MoS_2/Ti, TiO_2/Ti and $MoS_2/TiO_2/Ti$ were obtained, suggesting the surficial decoration with MoS_2, TiO_2, or MoS_2/TiO_2 could depress the recombination effectively [61]. This confirms the interface is in favor of the charge separation and transfer between the TiO_2 and Ti during the HER under the light.

In brief, the homo-junction on the substrate of Ti and Z-scheme hetero-junction play multiple roles during the whole HER. First, the homo-junction TiO_2 with narrow band gap can not only utilize visible light energy to excite the electrons from the VB to CB, but also acquire the hot electrons transferred at the interface of quasi-core-shell TiO_2/Ti [37–40]. The homo-junction forms an inter-phase junction to afford the band bending, and then favoring the excited electrons toward the hetero-junction interface. Second, the Z-scheme hetero-junction transports the electrons to the VB of MoS_2, where the electrons are then excited to the CB by the sunlight energy, further participating into the HER on the active sites of MoS_2. Furthermore, the Z-scheme connection provides excellent protection on the MoS_2 through directing the photo-excited holes in the VB of MoS_2 toward the hetero-junction interface space meeting with the electrons from the CB of TiO_2, preventing the MoS_2 from the photo-excited holes induced corrosion and therefore imparting a higher stability to the system [62]. In turn, the upper MoS_2 layer also acts as protective material for the underneath TiO_2. The low cost of Ti and MoS_2 with simply fabrication processes makes them favorable to demonstrate our hybrid-junction scheme. The optimization for the processes and manipulation should result in better HER performance and enhanced the visible light utilization, like modifying the thickness of MoS_2 [63–65].

4. Conclusions

Novel hybrid-junction $MoS_2/TiO_2/Ti$ photocathode was fabricated by a facile process that combines thermal oxidaiton and hand-spraying. This hybrid-junction photocathode under visible light exhibited improved HER activities, in which the overpotential required to obtain 10 mA cm^{-2} was reduced to -114 mV, as well as long-term stability was achieved for over more than 12 h at -0.3 V Vs RHE while in comparison the cathode without the introduction of hybrid-junction only persisted about 1 h under the same conditions. The associated homo-junction and Z-scheme hetero-junction were attributed to the enhanced charge carrier dynamics and reduced recombination, therefore improved HER activities under the light. Synthesized by simple one-step thermal oxidation process, the homo-junction TiO_2 on the substrate of Ti with plasmonic resonances and charge separation ability is supposed to have more wide range of application capability in sunlight energy-conversion systems. The concept of hybrid-junction provides a cost-economical strategy to regulate the charge carrier separation, transfer and transportation dynamics of photoelectrodes and catalysts that do hold poor characteristic under given working environment for practical solar water splitting.

Acknowledgement

The authors would like to acknowledge the support from Norwegian Research Council FRINATEK Programme (231416/F20), China Scholarship Council (CSC, Grant No. 201506930002), the Norwegian Micro- and Nano-Fabrication Facility (NorFab, project number 245963/F50), and a STSM Grant from To-BE COST Action (MP 1308) supported by COST (European Cooperation in Science and Technology). We also want to acknowledge the valuable help of Muhammad Tayyib who helped us in the characterization of SEM, EDX and EBSD.

Appendix A. Supplementary data

Supplementary material related to this article can be found, in the online version, at doi:https://doi.org/10.1016/j.apcatb.2018.06.012.

References

[1] O. Khaselev, A monolithic photovoltaic-photoelectrochemical device for hydrogen production via water splitting, Science 280 (1998) 425–427.
[2] Y. Tachibana, L. Vayssieres, J.R. Durrant, Artificial photosynthesis for solar water-splitting, Nat. Photonics 6 (2012) 511–518.
[3] D.M. Fabian, S. Hu, N. Singh, F.A. Houle, T. Hisatomi, K. Domen, F.E. Osterloh, S. Ardo, Particle suspension reactors and materials for solar-driven water splitting, Energy Environ. Sci. 8 (2015) 2825–2850.
[4] A. Landman, H. Dotan, G.E. Shter, M. Wullenkord, A. Houaijia, A. Maljusch, G.S. Grader, A. Rothschild, Photoelectrochemical water splitting in separate oxygen and hydrogen cells, Nat. Mater. 16 (2017) 646–651.
[5] R.M. Navarro, M.C. Alvarez-Galván, J.A. Villoria de la Mano, S.M. Al-Zahrani, J.L.G. Fierro, A framework for visible-light water splitting, Energy Environ. Sci. 3 (2010) 1865.
[6] J.H. Montoya, L.C. Seitz, P. Chakthranont, A. Vojvodic, T.F. Jaramillo, J.K. Norskov, Materials for solar fuels and chemicals, Nat. Mater. 16 (2016) 70–81.
[7] I. Roger, M.A. Shipman, M.D. Symes, Earth-abundant catalysts for electrochemical and photoelectrochemical water splitting, Nat. Rev. Chem. 1 (2017) 0003.
[8] L. Zhou, H. Zhang, H. Sun, S. Liu, M.O. Tade, S. Wang, W. Jin, Recent advances in non-metal modification of graphitic carbon nitride for photocatalysis: a historic review, Catal. Sci. Technol. 6 (2016) 7002–7023.
[9] F.F. Abdi, L. Han, A.H. Smets, M. Zeman, B. Dam, R. van de Krol, Efficient solar water splitting by enhanced charge separation in a bismuth vanadate-silicon tandem photoelectrode, Nat. Commun. 4 (2013) 2195 Khaselev.
[10] K.T. Fountaine, H.J. Lewerenz, H.A. Atwater, Efficiency limits for photoelectrochemical water-splitting, Nat. Commun. 7 (2016) 13706.
[11] H.M. Chen, C.K. Chen, R.S. Liu, L. Zhang, J. Zhang, D.P. Wilkinson, Nano-architecture and material designs for water splitting photoelectrodes, Chem. Soc. Rev. 41 (2012) 5654–5671.
[12] S.Y. Reece, J.A. Hamel, K. Sung, T.D. Jarvi, A.J. Esswein, J.J. Pijpers, D.G. Nocera, Wireless solar water splitting using silicon-based semiconductors and earth-abundant catalysts, Science 334 (2011) 645–648.
[13] J. Luo, J.H. Im, M.T. Mayer, M. Schreier, M.K. Nazeeruddin, N.G. Park, S.D. Tilley, H.J. Fan, M. Gratzel, Water photolysis at 12.3% efficiency via perovskite photovoltaics and earth-abundant catalysts, Science 345 (2014) 1593–1596.
[14] X. Li, J. Yu, J. Low, Y. Fang, J. Xiao, X. Chen, Engineering heterogeneous semiconductors for solar water splitting, J. Mater. Chem. A 3 (2015) 2485–2534.
[15] L. Yuan, C. Han, M.-Q. Yang, Y.-J. Xu, Photocatalytic water splitting for solar hydrogen generation: fundamentals and recent advancements, Int. Rev. Phys. Chem. 35 (2016) 1–36.
[16] H. Wang, L. Zhang, Z. Chen, J. Hu, S. Li, Z. Wang, J. Liu, X. Wang, Semiconductor heterojunction photocatalysts: design, construction, and photocatalytic performances, Chem. Soc. Rev. 43 (2014) 5234–5244.
[17] G. Liu, K. Du, S. Haussener, K. Wang, Charge transport in two-photon semiconducting structures for solar fuels, ChemSusChem 9 (2016) 2878–2904.
[18] Y. Liu, H. Zhang, J. Ke, J. Zhang, W. Tian, X. Xu, X. Duan, H. Sun, M.O. Tade, S. Wang, 0D (MoS_2)/2D (g-C_3N_4) heterojunctions in Z-scheme for enhanced photocatalytic and electrochemical hydrogen evolution, Appl. Catal. B. 228 (2018) 64–74.
[19] R. Abe, Recent progress on photocatalytic and photoelectrochemical water splitting under visible light irradiation, J. Photoch. Photobio. C 11 (2010) 179–209.
[20] T. Hisatomi, J. Kubota, K. Domen, Recent advances in semiconductors for photocatalytic and photoelectrochemical water splitting, Chem. Soc. Rev. 43 (2014)

7520–7535.
[21] R. Raja, P. Sudhagar, A. Devadoss, C. Terashima, L.K. Shrestha, K. Nakata, R. Jayavel, K. Ariga, A. Fujishima, Pt-free solar driven photoelectrochemical hydrogen fuel generation using 1T MoS_2 co-catalyst assembled CdS QDs/TiO_2 photoelectrode, Chem. Commun. (Camb.) 51 (2015) 522–525.
[22] Y. Pi, Z. Li, D. Xu, J. Liu, Y. Li, F. Zhang, G. Zhang, W. Peng, X. Fan, 1T-phase MoS_2 nanosheets on TiO_2 nanorod arrays: 3D photoanode with extraordinary catalytic performance, ACS sustain, Chem. Eng. 5 (2017) 5175–5182.
[23] X. Zhu, X. Liang, X. Fan, X. Su, Fabrication of flower-like MoS_2/TiO_2 hybrid as an anode material for lithium ion batteries, RSC Adv. 7 (2017) 38119–38124.
[24] J. Zhang, L. Zhang, W. Yu, F. Jiang, E. Zhang, H. Wang, Z. Kong, J. Xi, Z. Ji, Novel dual heterojunction between MoS_2 and anatase TiO_2 with coexposed {101} and {001} facets, J. Am. Ceram. Soc. 100 (2017) 5274–5285.
[25] B. Chen, Y. Meng, J. Sha, C. Zhong, W. Hu, N. Zhao, Preparation of MoS_2/TiO_2 based nanocomposites for photocatalysis and rechargeable batteries: progress, challenges, and perspective, Nanoscale 10 (2017) 34–68.
[26] H. He, J. Lin, W. Fu, X. Wang, H. Wang, Q. Zeng, Q. Gu, Y. Li, C. Yan, B.K. Tay, C. Xue, X. Hu, S.T. Pantelides, W. Zhou, Z. Liu, MoS_2/TiO_2 Edge-on heterostructure for efficient photocatalytic hydrogen evolution, Adv. Energy Mater. 6 (2016) 1600464.
[27] L. Guo, Z. Yang, K. Marcus, Z. Li, B. Luo, L. Zhou, X. Wang, Y. Du, Y. Yang, MoS_2/TiO_2 heterostructures as nonmetal plasmonic photocatalysts for highly efficient hydrogen evolution, Energy Environ. Sci. 11 (2018) 106–114.
[28] W.K. Wang, J.J. Chen, X. Zhang, Y.X. Huang, W.W. Li, H.Q. Yu, Self-induced synthesis of phase-junction TiO_2 with a tailored rutile to anatase ratio below phase transition temperature, Sci. Rep. 6 (2016) 20491.
[29] A. Li, Z. Wang, H. Yin, S. Wang, P. Yan, B. Huang, X. Wang, R. Li, X. Zong, H. Han, C. Li, Understanding the anatase–rutile phase junction in charge separation and transfer in a TiO_2 electrode for photoelectrochemical water splitting, Chem. Sci. 7 (2016) 6076–6082.
[30] Y. Zhao, N. Hoivik, K. Wang, Recent advance on engineering titanium dioxide nanotubes for photochemical and photoelectrochemical water splitting, Nano Energy 30 (2016) 728–744.
[31] F.F. Abdi, L. Han, A.H. Smets, M. Zeman, B. Dam, R. van de Krol, Efficient solar water splitting by enhanced charge separation in a bismuth vanadate-silicon tandem photoelectrode, Nat. Commun. 4 (2013) 2195.
[32] N. Wang, M. Liu, H. Tan, J. Liang, Q. Zhang, C. Wei, Y. Zhao, E.H. Sargent, X. Zhang, Compound homojunction: heterojunction reduces bulk and interface recombination in ZnO photoanodes for water splitting, Small 13 (2017).
[33] Z. Zhang, Y. Huang, K. Liu, L. Guo, Q. Yuan, B. Dong, Multichannel-improved charge-carrier dynamics in well-designed hetero-nanostructural plasmonic photocatalysts toward highly efficient solar-to-fuels conversion, Adv. Mater. 27 (2015) 5906–5914.
[34] Y.H. Tseng, C.S. Kuo, C.H. Huang, Y.Y. Li, P.W. Chou, C.L. Cheng, M.S. Wong, Visible-light-responsive nano-TiO(2) with mixed crystal lattice and its photocatalytic activity, Nanotechnology 17 (2006) 2490–2497.
[35] M.A. Mohamed, W.N. Wan Salleh, J. Jaafar, N. Yusof, Preparation and photocatalytic activity of mixed phase anatase/rutile TiO_2 nanoparticles for phenol degradation, Jurnal Teknologi (2014) 70.
[36] S. Yeniyol, I. Mutlu, Z. He, B. Yuksel, R.J. Boylan, M. Urgen, Z.C. Karabuda, C. Basegmez, J.L. Ricci, Photocatalytical antibacterial activity of mixed-phase TiO_2 nanocomposite thin films against Aggregatibacter actinomycetemcomitans, BioMed Res. Int. (2015) (2015) 705871.
[37] R. Jiang, B. Li, C. Fang, J. Wang, Metal/Semiconductor hybrid nanostructures for plasmon-enhanced applications, Adv. Mater. 26 (2014) 5274–5309.
[38] Y. Pihosh, I. Turkevych, K. Mawatari, N. Fukuda, R. Ohta, M. Tosa, K. Shimamura, E.G. Villora, T. Kitamori, Ubiquitous element approach to plasmonic enhanced photocatalytic water splitting: the case of Ti@TiO_2 core-shell nanostructure, Nanotechnology 25 (2014) 315402.
[39] G. Liu, K. Du, J. Xu, G. Chen, M. Gu, C. Yang, K. Wang, H. Jakobsen, Plasmon-dominated photoelectrodes for solar water splitting, J. Mater. Chem. A 5 (2017) 4233–4253.
[40] S. Tan, A. Argondizzo, J. Ren, L. Liu, J. Zhao, H. Petek, Plasmonic coupling at a metal/semiconductor interface, Nat. Photonics 11 (2017) 806–812.
[41] M.W. Knight, N.S. King, L. Liu, H.O. Everitt, P. Nordlander, N.J. Halas, Aluminum for plasmonics, ACS Nano 8 (2014) 834–840.
[42] N.T. Thomas, K. Nobe, Kinetics of the hydrogen evolution reaction on titanium, J. Electrochem. Soc. 117 (1970) 622.
[43] D. Kiriya, P. Lobaccaro, H.Y. Nyein, P. Taheri, M. Hettick, H. Shiraki, C.M. Sutter-Fella, P. Zhao, W. Gao, R. Maboudian, J.W. Ager, A. Javey, General thermal texturization process of MoS_2 for efficient electrocatalytic hydrogen evolution reaction, Nano Lett. 16 (2016) 4047–4053.
[44] X. Zou, Y. Zhang, Noble metal-free hydrogen evolution catalysts for water splitting, Chem. Soc. Rev. 44 (2015) 5148–5180.
[45] J. Kibsgaard, Z. Chen, B.N. Reinecke, T.F. Jaramillo, Engineering the surface structure of MoS_2 to preferentially expose active edge sites for electrocatalysis, Nat. Mater. 11 (2012) 963–969.
[46] X. Hai, W. Zhou, K. Chang, H. Pang, H. Liu, L. Shi, F. Ichihara, J. Ye, Engineering the crystallinity of MoS_2 monolayers for highly efficient solar hydrogen production, J. Mater. Chem. A 5 (2017) 8591–8598.
[47] K. Chang, H. Pang, X. Hai, G. Zhao, H. Zhang, L. Shi, F. Ichihara, J. Ye, Ultra-small freestanding amorphous molybdenum sulfide colloidal nanodots for highly efficient photocatalytic hydrogen evolution reaction, Appl. Catal. B. 232 (2018) 446–453.
[48] C. Tan, Z. Luo, A. Chaturvedi, Y. Cai, Y. Du, Y. Gong, Y. Huang, Z. Lai, X. Zhang, L. Zheng, X. Qi, M.H. Goh, J. Wang, S. Han, X.J. Wu, L. Gu, C. Kloc, H. Zhang, Preparation of high-percentage 1T-phase transition metal dichalcogenide nanodots for electrochemical hydrogen evolution, Adv. Mater. 30 (2018) e1705509.
[49] M.A.R. Anjum, H.Y. Jeong, M.H. Lee, H.S. Shin, J.S. Lee, Efficient hydrogen evolution reaction catalysis in alkaline media by all-in-one MoS_2 with multifunctional active sites, Adv. Mater. 30 (2018) e1707105.
[50] E. Parzinger, B. Miller, B. Blaschke, J.A. Garrido, J.W. Ager, A. Holleitner, U. Wurstbauer, Photocatalytic stability of single- and few-layer MoS(2), ACS Nano 9 (2015) 11302–11309.
[51] T. Lopes, L. Andrade, H.A. Ribeiro, A. Mendes, Characterization of photoelectrochemical cells for water splitting by electrochemical impedance spectroscopy, Int. J. Hydrogen Energy 35 (2010) 11601–11608.
[52] M.I.D.-Ga.R. Gómez, Investigating water splitting with $CaFe_2O_4$ photocathodes by electrochemical impedance spectroscopy, ACS Appl. Mater. Interfaces 8 (2016) 11.
[53] Y.-J. Yuan, Z.-J. Ye, H.-W. Lu, B. Hu, Y.-H. Li, D.-Q. Chen, J.-S. Zhong, Z.-T. Yu, Z.-G. Zou, Constructing anatase TiO_2 nanosheets with exposed (001) facets/layered MoS_2 two-dimensional nanojunctions for enhanced solar hydrogen generation, ACS Catal. 6 (2015) 532–541.
[54] D.O. Scanlon, C.W. Dunnill, J. Buckeridge, S.A. Shevlin, A.J. Logsdail, S.M. Woodley, C.R. Catlow, M.J. Powell, R.G. Palgrave, I.P. Parkin, G.W. Watson, T.W. Keal, P. Sherwood, A. Walsh, A.A. Sokol, Band alignment of rutile and anatase TiO(2), Nat. Mater. 12 (2013) 798–801.
[55] N. Baram, Y. Ein-Eli, Electrochemical impedance spectroscopy of porous TiO_2 for photocatalytic applications, J. Phys. Chem. C 114 (2010) 9781–9790.
[56] L. Cao, R. Wang, D. Wang, X. Li, H. Jia, MoS_2 -hybridized TiO_2 nanosheets with exposed {001} facets to enhance the visible-light photocatalytic activity, Mater. Lett. 160 (2015) 286–290.
[57] J. Tao, J. Chai, L. Guan, J. Pan, S. Wang, Effect of interfacial coupling on photocatalytic performance of large scale MoS_2/TiO_2 hetero-thin films, Appl. Phys. Lett. 106 (2015) 081602.
[58] D. Wang, Y. Xu, F. Sun, Q. Zhang, P. Wang, X. Wang, Enhanced photocatalytic activity of TiO_2 under sunlight by MoS_2 nanodots modification, Appl. Surf. Sci. 377 (2016) 221–227.
[59] X. Liu, Z. Xing, Y. Zhang, Z. Li, X. Wu, S. Tan, X. Yu, Q. Zhu, W. Zhou, Fabrication of 3D flower-like black n-TiO_{2-x} @MoS_2 for unprecedented-high visible-light-driven photocatalytic performance, Appl. Catal. B: Environ. 201 (2017) 119–127.
[60] Z. Jiang, W. Wan, H. Li, S. Yuan, H. Zhao, P.K. Wong, A hierarchical Z-scheme alpha-FeO_3/g-C_3N_4 hybrid for enhanced photocatalytic CO_2 reduction, Adv. Mater. 30 (10) (2018) e1706108.
[61] X. Yang, H. Huang, B. Jin, J. Luo, X. Zhou, Facile synthesis of MoS_2/B-TiO_2 nanosheets with exposed {001} facets and enhanced visible-light-driven photocatalytic H_2 production activity, RSC Adv. 6 (2016) 107075–107080.
[62] Y. Yang, Y. Ling, G. Wang, T. Liu, F. Wang, T. Zhai, Y. Tong, Y. Li, Photohole induced corrosion of titanium dioxide: mechanism and solutions, Nano Lett. 15 (2015) 7051–7057.
[63] D. McAteer, Z. Gholamvand, N. McEvoy, A. Harvey, E. O'Malley, G.S. Duesberg, J.N. Coleman, Thickness dependence and percolation scaling of hydrogen production rate in MoS_2 nanosheet and nanosheet-carbon nanotube composite catalytic electrodes, ACS Nano 10 (2016) 672–683.
[64] Y. Zhang, H. Li, H. Wang, H. Xie, R. Liu, S.L. Zhang, Z.J. Qiu, Thickness considerations of two-dimensional layered semiconductors for transistor applications, Sci. Rep. 6 (2016) 29615.
[65] A. Sohn, H. Moon, J. Kim, M. Seo, K.-A. Min, S.W. Lee, S. Yoon, S. Hong, D.-W. Kim, Band alignment at Au/MoS_2 contacts: thickness dependence of exfoliated flakes, J. Phys. Chem. C 121 (2017) 22517–22522.